

The Heavy Photon Search Test Detector

M. Battaglieri^a, S. Boyarinov^b, S. Buelmann^c, V. Burkert^b, G. Charles^d, W. Cooper^e, N. Dashyan^f, R. De Vita^a, A. Deur^b, R. Dupre^d, H. Egiyan^b, L. Elouadrhiri^b, R. Essig^g, V. Fadeyev^h, C. Fieldⁱ, A. Freyberger^b, N. Gevorgyan^f, F.-X. Girod^b, N. Grafⁱ, M. Grahamⁱ, K. Griffioen^j, A. Grillo^h, M. Guidal^d, G. Hallerⁱ, P. Hansson Adrian^{i,*}, R. Herbstⁱ, M. Holtrop^k, J. Jarosⁱ, S. K. Phillips^k, M. Khandaker^l, A. Kubarovskiy^m, T. Maruyamaⁱ, J. McCormickⁱ, K. Moffeitⁱ, O. Moreno^h, H. Nealⁱ, T. Nelsonⁱ, S. Niccolai^d, A. Odianⁱ, M. Oriunnoⁱ, R. Paremuzyan^f, E. Rauly^d, E. Rindel^d, P. Rosier^d, C. Salgado^l, P. Schusterⁿ, Y. Sharabian^b, K. Slifer^k, D. Sokhan^o, S. Stepanyan^b, P. Stoler^m, N. Toroⁿ, S. Uemuraⁱ, M. Ungaro^b, H. Voskanyan^f, D. Walzⁱ, L. B. Weinstein^c, B. Wojtsekhowski^b

^aIstituto Nazionale di Fisica Nucleare, Sezione di Genova e Dipartimento di Fisica dell'Università, 16146 Genova, Italy

^bThomas Jefferson National Accelerator Facility, Newport News, Virginia 23606

^cOld Dominion University, Norfolk, Virginia 23529

^dInstitut de Physique Nucléaire d'Orsay, IN2P3, BP 1, 91406 Orsay, France

^eFermi National Accelerator Laboratory, Batavia, IL 60510-5011

^fYerevan Physics Institute, 375036 Yerevan, Armenia

^gStony Brook University, Stony Brook, NY 11794-3800

^hUniversity of California, Santa Cruz, CA 95064

ⁱSLAC National Accelerator Laboratory, Menlo Park, CA 94025

^jThe College of William and Mary, Department of Physics, Williamsburg, VA 23185

^kUniversity of New Hampshire, Department of Physics, Durham, NH 03824

^lNorfolk State University, Norfolk, Virginia 23504

^mRensselaer Polytechnic Institute, Department of Physics, Troy, NY 12181

ⁿPerimeter Institute, Ontario, Canada N2L 2Y5

^oUniversity of Glasgow, Glasgow, G12 8QQ, Scotland, UK

Abstract

The Heavy Photon Search (HPS), an experiment to search for a hidden sector photon in fixed target electroproduction, is preparing for installation at the Thomas Jefferson National Accelerator Facility (JLab) in the Fall of 2014. As the first stage of this project, the HPS Test Run apparatus was constructed and operated in 2012 to demonstrate the experiment's technical feasibility and to confirm that the trigger rates and occupancies are as expected. This paper describes the HPS Test Run apparatus and readout electronics and its performance. In this setting, a heavy photon can be identified as a narrow peak in the e^+e^- invariant mass spectrum, above the trident background or as a narrow invariant mass peak with a decay vertex displaced from the production target, so charged particle tracking and vertexing are needed for its detection. In the HPS Test Run, charged particles are measured with a compact forward silicon microstrip tracker inside a dipole magnet. Electromagnetic showers are detected in a PbWO₄ crystal calorimeter situated behind the magnet used to trigger the experiment and identify electrons and positrons. Both detectors are placed close to the beam line and split top-bottom. This arrangement provides sensitivity to low-mass heavy photons, allows clear passage of the unscattered beam, and avoids the spray of degraded electrons coming from the target. The discrimination between prompt and displaced e^+e^- pairs requires the first layer of silicon sensors be placed only 10 cm downstream of the target. The expected signal is small, and the trident background huge, so the experiment requires very large statistics. Accordingly, the HPS Test Run utilizes high-rate readout and data acquisition electronics and a fast trigger to exploit the essentially 100% duty cycle of the CEBAF accelerator at JLab.

Keywords: silicon microstrip, tracking, vertexing, heavy photon, dark photon, hidden sector, electromagnetic calorimeter

*Corresponding author.

Email address: phansson@slac.stanford.edu (P. Hansson)

Adrian)

1 **Contents**

2	1	Introduction	3
3	2	Detector Overview	3
4	3	The HPS Test Run Beamline	5
5	4	Silicon Vertex Tracker	5
6	4.1	Layout	6
7	4.2	Components	6
8	4.3	Production, Assembly and Shipping . .	7
9	4.4	Alignment	7
10	5	Electromagnetic Calorimeter	8
11	5.1	Components	8
12	5.2	Layout	8
13	5.3	Signal readout	8
14	6	Trigger and Data Acquisition	9
15	6.1	Trigger system	9
16	6.2	SVT Data Acquisition	9
17	6.3	General Data Acquisition and Online Computing	10
19	7	Reconstruction and Performance	10
20	7.1	SVT Performance	10
21	7.1.1	Cluster and Hit Reconstruction .	11
22	7.1.2	Momentum and Vertexing Res- olution	12
23	7.2	ECal Performance	12
24	7.3	Trigger Performance	14
25	7.4	Trigger Rate Comparisons	14
27	8	Summary and Outlook	14
28	9	Acknowledgements	15

29 **1. Introduction**

30 The heavy photon (A'), aka a “hidden sector” or
31 “dark” photon, is a particle with mass $10 - 1000 \text{ MeV}/c^2$
32 which couples weakly to electric charge by mixing with
33 the Standard Model photon [1]. Consequently, it can
34 be radiated by electrons and subsequently decay into
35 e^+e^- pairs, albeit at rates far below those of QED trident
36 processes. Heavy photons have been suggested by nu-
37 merous beyond Standard Model theories [2], to explain
38 the discrepancy between theory and experiment of the
39 muon’s $g - 2$ [3], and as a possible explanation of recent
40 astrophysical anomalies [4, 5, 6]. Heavy photons couple
41 directly to hidden sector particles with “dark” or “hid-
42 den sector” charge; these particles could constitute all
43 or some of the dark matter [7]. Current phenomenology
44 highlights the $20 - 1000 \text{ MeV}/c^2$ mass range, and sug-
45 gests that the coupling to electric charge, ϵe , has ϵ in the
46 range of $10^{-3} - 10^{-5}$. This range of parameters makes
47 A' searches viable in medium energy fixed target elec-
48 troproduction [8], but requires large data sets and good
49 mass resolution to identify a small mass peak above the
50 copious QED background. At small couplings, A' be-
51 come long-lived, so detection of a displaced decay ver-
52 tex can reject the prompt QED background and boost
53 experimental sensitivity.

54 The HPS experiment [9] uses both invariant mass and
55 secondary vertex signatures to search for A' . It uses a
56 $\approx 1 \text{ m}$ long silicon tracking and vertexing detector in-
57 side a dipole magnet to measure charged particle trajec-
58 tories and a fast electromagnetic calorimeter just down-
59 stream of the magnet to provide a trigger and identify
60 electrons. The experiment utilizes very high-rate front-
61 end electronics and runs at high trigger rates (up to
62 50kHz), exploiting the 100% duty cycle of the JLab CE-
63 BAF accelerator to accumulate the needed statistics.

64 The HPS Test Run, using a simplified version of the
65 HPS apparatus, was proposed and approved at JLab as
66 the first stage of HPS. Its purposes included demon-
67 strating that the apparatus and data acquisition systems are
68 technically feasible and the trigger rates and occupan-
69 cies to be encountered in electron-beam running are as
70 simulated. Given dedicated running time with electron
71 beams, the HPS Test Run apparatus is capable of search-
72 ing for heavy photons in unexplored regions of parame-
73 ter space. The key design criteria for HPS and the HPS
74 Test Run are the same:

- 75 • large and uniform acceptance in the forward region
76 close to the beam in order to catch boosted A' de-
77 cay products,
- 78 • beam passage through the apparatus in vacuum, to

79 eliminate direct interactions with the detector and
80 minimize beam gas interactions,

- 81 • detector components that can survive and effi-
82 ciently operate in a high radiation environment
83 with local doses exceeding 100 Mrad.
- 84 • high-rate electronics with excellent timing resolu-
85 tion to minimize out of time backgrounds,
- 86 • a flexible, redundant and efficient trigger selecting
87 electron and positron pairs at rates up to 50 kHz,
- 88 • data handling rates of 100 MB/s to permanent stor-
89 age,
- 90 • excellent track reconstruction efficiency for elec-
91 trons and positrons,
- 92 • good angular and momentum resolution to recon-
93 struct invariant mass precisely,
- 94 • excellent vertex resolution to discriminate dis-
95 placed A' decays from prompt QED backgrounds,

96 The HPS Test Run apparatus was installed on April
97 19, 2012, and ran parasitically in the photon beam of
98 the HDice experiment [10] until May 18. The JLab
99 run schedule precluded any dedicated electron beam
100 running, but the HPS Test Run was allowed a short
101 and valuable dedicated photon beam run at the end of
102 scheduled CEBAF running. This final running provided
103 enough data to demonstrate the functionality of the ap-
104 paratus, document its performance, and explore trigger
105 rates, as shown below.

106 This paper reviews the HPS Test Run apparatus, doc-
107 umenting the performance of the trigger, data acqui-
108 sition, silicon tracking detector, and the electromag-
109 netic calorimeter at the level required for calculating the
110 physics reach of the HPS experiment.

111 **2. Detector Overview**

112 The HPS Test Run apparatus was designed to run
113 in Hall B at JLab using the CEBAF 499MHz electron
114 beam at energies between 2.2 and 6.6 GeV and cur-
115 rents between 200 and 600 nA. The overall design of
116 the experiment follows from the kinematics of A' pro-
117 duction which typically results in a final state particle
118 within a few degrees of the incoming beam, especially
119 at low $m_{A'}$. Detectors must therefore be placed close
120 to the beam. The intense electron beam enlarges down-
121 stream after multiple scattering in the target and elec-
122 trons which have radiated in the target disperse horizon-
123 tally in the field of the analyzing magnet. Together they

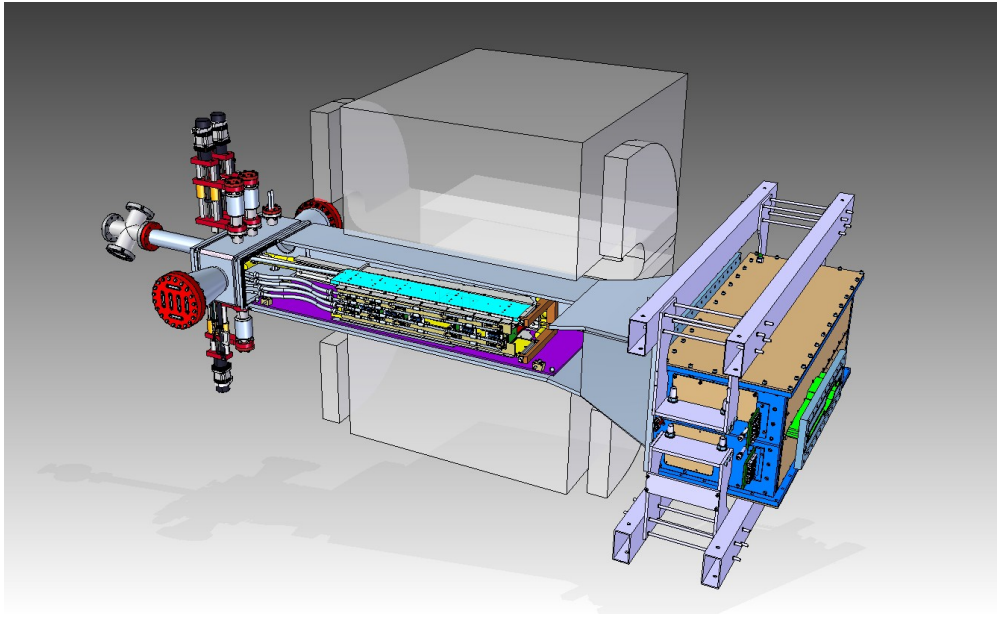


Figure 1: Rendering of the HPS Test Run apparatus installed on the beam line.

124 constitute a “wall of flame” which must be completely
 125 avoided. Accordingly, the apparatus is split vertically
 126 to avoid a “dead zone”, the region within ± 15 mrad of
 127 the beam plane. In addition, the beam is transported in
 128 vacuum through the tracker to minimize beam-gas inter-
 129 action backgrounds. Even with these precautions, the
 130 occupancies of sensors near the beam plane are high,
 131 dominated by the multiple Coulomb scattering of the
 132 primary beam, so high-rate detectors, a fast trigger, and
 133 excellent time tagging are required to minimize their
 134 impact. The trigger comes from a highly-segmented
 135 lead-tungstate (PbWO_4) crystal calorimeter located just
 136 downstream of the dipole magnet.

137
 138 A rendering of the apparatus installed on the beam line
 139 is shown in Figure 1 and an overview of the coverage,
 140 segmentation and performance is given in Table 1.

141 The silicon vertex tracking and vertexing detector for
 142 the HPS Test Run, or SVT, resides in a vacuum cham-
 143 ber inside the Pair Spectrometer (PS) dipole magnet in
 144 Hall B at JLab. The magnetic field strength was 0.5 T
 145 oriented vertically throughout the run. The SVT has
 146 five measurement stations, or “layers,” beginning 10 cm
 147 downstream of the target. Each layer comprises a pair
 148 of closely-spaced silicon microstrip sensors responsi-
 149 ble for measuring a single coordinate, or “view”. In-
 150 troduction of a small (50 or 100 mrad) stereo angle

151 between the two sensors of each layer provides three-
 152 dimensional tracking and vertexing throughout the ac-
 153 ceptance of the detector. In order to accommodate the
 154 dead zone, the SVT is built in two halves that are ap-
 155 proximately mirror reflections of one another about the
 156 plane of the nominal electron beam. Each layer in one
 157 half is supported on a common support plate with inde-
 158 pendent cooling and readout.

159
 160 The electromagnetic calorimeter (ECal) is also split
 161 into two halves. Each half of the ECal consists of
 162 221 PbWO_4 crystals arranged in rectangular formation.
 163 There are five rows with 46 modules in each row except
 164 the row closest to the beam plane which has 37. The
 165 light from each crystal is read out by an Avalanche Pho-
 166 todioide (APD) glued on the back surface of the crys-
 167 tal. Signals from the APDs are amplified using custom-
 168 made amplifier boards before being sent to the data ac-
 quisition electronics.

169 The Data Acquisition system combines two architec-
 170 tures, the Advanced Telecom Communications Archi-
 171 tecture (ATCA) based SVT readout system and VME-
 172 bus Switched Serial (VXS) based digitization and trig-
 173 gering system for the ECal. The system was designed
 174 to run at up to 20 kHz trigger rate.

Table 1: Overview of the coverage, segmentation and performance of the HPS Test Run detector.

System	Coverage (mrad)	# channels	ADC (bit)	Time resolution (ns)	# layers	Segmentation	Performance
SVT	$15 < \theta_y < 70$ (5 hits)	12780	14	≈ 2 ns	5 (stereo layers)	$\approx 120 \mu\text{m} r - \phi$ $\approx 6 \mu\text{m} z$	$\sigma_{d0,y} \approx 100 \mu\text{m}$ $\sigma_{d0,x} \approx 300 \mu\text{m}$ $\sigma_{d0,z} \approx 1 \text{ mm}$
Ecal	$15 < \theta_y < 60$	442	12	4 ns	1	$1.33 \times 1.33 \text{ cm}^2$ $1.6 \times 1.6 \text{ cm}^2$	$\sigma(E)/E \approx 4.5\%$

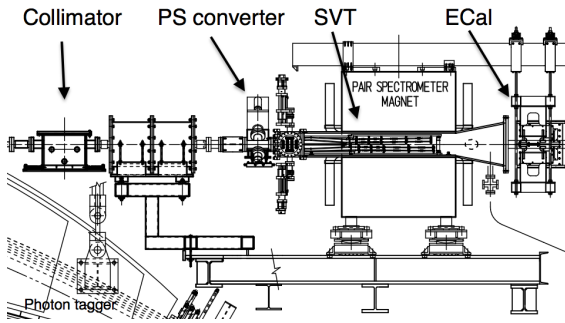


Figure 2: Layout of the HPS parasitic run.

175 3. The HPS Test Run Beamline

176 Since an electron beam was unavailable, the HPS Test
177 Run detected the electrons and positrons produced by
178 interactions of the secondary photon beam with a thin
179 foil just upstream of the detectors. The HPS Test Run
180 studied the performance of the detectors and the mul-
181 tiple coulomb scattering of the electrons and positrons.
182 Figure 2 shows the layout of the setup on the beam line.
183 The SVT was installed inside the Hall B pair spectrom-
184 ete magnet vacuum chamber with the ECal mounted
185 downstream of it. Both the SVT and the ECal were re-
186 tracted off the beam plane compared to nominal electron
187 beam running to allow clean passage of the photon beam
188 through the system.

189 The photon beam was generated in the interaction of
190 5.5 GeV electrons with a $10^{-4} X_0$ gold radiator located
191 ≈ 9 m upstream of the PS. The primary beam and scat-
192 tered electrons are deflected away from detectors by the
193 dipole magnet of the photon tagging system. During the
194 dedicated HPS Test Run period, the collimated (6.4 mm
195 diameter) photon beam passes through the PS pair con-
196 verter gold foil and later the HPS system. The PS pair
197 converter was located ≈ 77 cm upstream of the first
198 layer of the SVT.

199 Data was taken on three different converter thick-
200 nesses with photon fluxes between 0.4 and $1.3 \times 10^8/\text{s}$
201 at photon energies between 0.55 and 5.5 GeV produced
202 by a 30 to 90 nA electron beam. Data was measured

Converter thickn. (% X_0)	Duration (s)	e^- on radiator (μC)
0	1279	88.1
0.18	2640	193.5
0.45	2149	140.7
1.6	911	24.4

Table 2: Measured integrated currents for the dedicated photon runs.

203 for both polarities of the PS dipole magnet.’ The photon
204 beam line during the HPS Test Run produced a rela-
205 tively large number of e^+e^- pairs originating upstream
206 of the converter position. This contribution was mea-
207 sured during data taking with “empty” converter runs,
208 i.e. removing the converter but with all other conditions
209 the same. The runs taken during the time dedicated to
210 HPS Test Run is summarized in Table 2.

211 4. Silicon Vertex Tracker

212 The Silicon Vertex Tracker (SVT) enables efficient
213 reconstruction of charged particles and precise determi-
214 nation of their trajectories. These measurements allow
215 A' decays to be distinguished from background via sim-
216 ultaneous estimation of the invariant mass of e^+e^- de-
217 cay products and the position of decay vertexes down-
218 stream of the target.

219 The design of the SVT is primarily driven by direct
220 physics requirements and constraints from the environ-
221 ment at the interaction region. The A' decay products
222 have momenta in the range of 1 GeV, so multiple scat-
223 tering dominates mass and vertexing uncertainties for
224 any possible material budget. The SVT must therefore
225 minimize the amount of material in the tracking vol-
226 ume. The signal yield for long-lived A' is very small,
227 so the rejection of prompt vertices must be exceedingly
228 pure, on the order of 10^{-7} , in order to eliminate all
229 prompt backgrounds. To achieve the required vertexing
230 performance the first layer of the SVT must be placed
231 no more than about 10 cm downstream of the target.
At that distance, it is found that the active region of

233 a sensor can be placed as close as 1.5 mm from the
 234 center of the beam, defining the 15 mrad “dead zone”
 235 mentioned previously, to maximize low-mass A’ ac-
 236 ceptance with decay products nearly collinear with the
 237 beam axis. At the edge of this “dead zone”, the radiation
 238 dose approaches 10^{15} electrons/cm²/month, or roughly
 239 3×10^{14} 1 MeV neutron equivalent/cm²/month [11], re-
 240 quiring the sensors to be actively cooled. Meanwhile,
 241 very low-energy delta rays from beam-gas interactions
 242 multiply the density of background hits, so the SVT
 243 must operate inside the beam vacuum. Finally, in or-
 244 der to protect the sensors, the detector must be movable
 245 so that it can be retracted during periods of uncertain
 246 beam conditions.

247 4.1. Layout

248 The layout of the SVT is summarized in Table 4.1 and
 249 rendered in Figure 3. Each of the layers is comprised
 250 of a pair of closely-spaced silicon microstrip sensors
 251 mounted back-to-back to form a module. A 100 mrad
 252 stereo angle is used in the first three layers to provide
 253 higher-resolution 3D space points for vertexing. Using
 254 50 mrad in the last two layers breaks the tracking de-
 255 generacy of having five identical layers and minimizes
 256 fakes from ghost hits to improve pattern recognition.
 257 Altogether, the SVT has 20 sensors for a total of 12780
 258 readout channels.

Layer	1	2	3	4	5
<i>z</i> from target (cm)	10	20	30	50	70
Stereo angle (mrad)	100	100	100	50	50
Bend res. (μm)	≈ 60	≈ 60	≈ 60	≈ 120	≈ 120
Non-bend res. (μm)	≈ 6	≈ 6	≈ 6	≈ 6	≈ 6
# of sensors	4	4	4	4	4
Dead zone (mm)	± 1.5	± 3.0	± 4.5	± 7.5	± 10.5
Power cons. (W)	6.9	6.9	6.9	6.9	6.9

259 Table 3: Layout of the SVT.

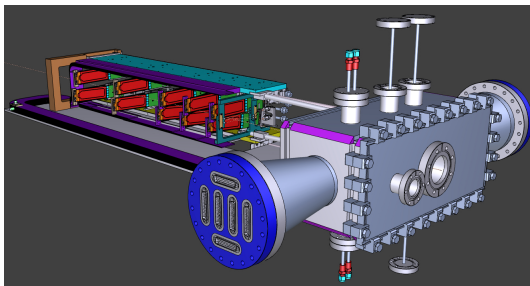


Figure 3: A rendering of the SVT showing the modules on their support plates held by the hinged C-support on the left and the motion levers on the right. The sensors are shown in red and the hybrid readout boards in green. The beam enters from the right through a vacuum box with flanges for services.

260
 261 The SVT is built in two separate halves that are mirror
 262 reflections of one another about the plane of the nom-
 263 inal electron beam. Each half consists of five modules
 264 mounted on a support plate that provides services to the
 265 modules and allows them to be moved as a group rel-
 266 ative to the dead zone. The two halves of the tracker
 267 are connected to hinges mounted on a C-shaped support
 268 just beyond the last layer that defines the nominal spac-
 269 ing between the upper and lower halves of the tracker.
 270 A shaft attached to each support plate in front of layer
 271 1 extends upstream and connects to a linear shift that
 272 transfers motion into the vacuum box through bellows
 273 to open and close the two halves around the dead zone.
 274 The C-support is mounted to an aluminum baseplate
 275 that defines the position of the SVT with respect to the
 276 vacuum chamber. Figure 4 shows a photograph of both
 completed detector halves prior to final assembly.



Figure 4: Both halves of the HPS Test Run SVT after final assembly at SLAC. The cooling manifolds and integrated cable runs are clearly seen.

277 4.2. Components

278 The sensors for the SVT are *p*-on-*n*, single sided,
 279 AC coupled, polysilicon-biased microstrip sensors fab-
 280 ricated on <100> silicon and have 30 (60) μm sense
 281 (readout) pitch over their $4 \times 10 \text{ cm}^2$ surface. This
 282 sensor technology was selected to match the require-
 283 ment of <1% X_0 per layer, single-hit resolution better
 284 than 50 μm and tolerance of a radiation dose of ap-
 285 proximately 1.5×10^{14} 1 MeV neutron equivalent/cm²
 286 for a six month run. The sensors were purchased from
 287 the Hamamatsu Photonics Corporation for the cancelled
 288 Run 2b upgrade of the DØ experiment [12] which satis-
 289 fied the requirement that the technology must be mature
 290 and available within the time and budget constraints.

Despite having only small spots with very high occupancy (up to 4 MHz/mm^2) closest to the primary beam, the rates are still high and lowering the peak occupancy to approximately 1% for tracking requires a trigger window and hit time tagging of roughly 8 ns. The ECal readout and trigger described in Sec. 5.3 can achieve such resolution. To reach this performance the sensors for the SVT are readout by the APV25 ASIC developed for the CMS experiment at CERN [13]. The APV25 can capture successive samples of the shaper output in groups of three at a sampling rate of approximately 40 MHz. By fitting the known *CR-RC* shaping curve to these samples, the initial time of the hit can be determined to a precision of 2 ns for $S/N \approx 25$ [14]. For electron beam running, six-sample readout and the shortest possible shaping time (35 ns) is used to best distinguish hits that overlap in time. The APV25 ASICs are hosted on simple FR4 hybrid readout boards, outside the tracking volume, with a short twisted-pair pigtail cable to provide power and configuration and signal readout. Along with a single sensor, these are glued to a polyamide-laminated carbon fiber composite backing making up a half-module. A window is machined in the carbon fiber leaving only a frame around the periphery of the silicon to minimize material. A $50 \mu\text{m}$ sheet of polyamide is laminated to the surface of the carbon fiber with 1 mm overhang at all openings to ensure good isolation between the backside of the sensor, carrying high-voltage bias, and the carbon fiber which is held near ground.

The sensor modules for the SVT consist of a pair of identical half-modules, sandwiched back-to-back around an aluminum cooling block at one end and a similar PEEK spacer block at the other. Figure 5 shows a single module after assembly. The cooling block pro-

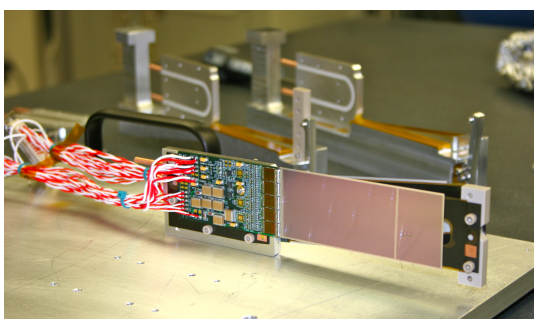


Figure 5: A prototype module assembly (foreground) with the 50 mrad (left) and 100 mrad (right) module assembly fixtures in the background. A pair of cooling blocks and a spacer block can be seen on the fixtures.

vides the primary mechanical support for the module as

well as cooling via copper tubes pressed into grooves in the plates. The spacer block defines the spacing between the sensors at the far end of the module, stiffens the module structure, and improves the stability of the sensor alignment. The average support material in the tracking volume is approximately $0.06\% X_0$ per double-sided module for a total material budget of 0.7% per layer.

The total SVT power consumption budget of about 50 W is removed by a water/glycol mixture circulated through a flexible manifold attached to the copper tubes in the cooling blocks. During the HPS Test Run the sensors were operated at around 23°C . The power consumption is dominated by five APV25 ASICs on each hybrid board consuming approximately 2 W, radiant heat load is less than 0.5 W per sensor and leakage current is only significant in a small spot after irradiation.

4.3. Production, Assembly and Shipping

Hybrids with APV25 ASICs underwent quick qualification testing and each half-module was run at low temperature ($\approx 5^\circ \text{C}$) and fully characterized for pedestals, gains, noise and time response after assembly. Of 29 half-modules built, 28 passed qualification testing, leaving 8 spare modules after completion of the SVT, all capable of 1000 V bias voltage without breakdown. Full-module assembly and mechanical surveys were performed at SLAC before final assembly, testing and shipping of the SVT to JLab. A custom shipping container with nested crates and redundant isolation for shock and vibration was built in order to safely send the partly assembled SVT to JLab. At JLab, the entire SVT was integrated with the full DAQ and the power supplies before moving the module-loaded support plates to Hall B for final mechanical assembly and installation inside of the vacuum chamber.

4.4. Alignment

The SVT was aligned using a combination of optical, laser and touch probe surveys at SLAC and JLab. The optical survey of individual modules with a precision of a few μm was combined with a touch-probe survey of the overall SVT support structure, with 25-100 μm precision, to locate the silicon sensor layers with respect to the support plates and the mechanical survey balls on the base plate. After full assembly and installation of the SVT at JLab, a mechanical survey of the SVT base plate position inside the pair spectrometer vacuum chamber is used to determine the global position of the SVT with respect to the CEBAF beam line. The resulting survey-based alignment has the position of the

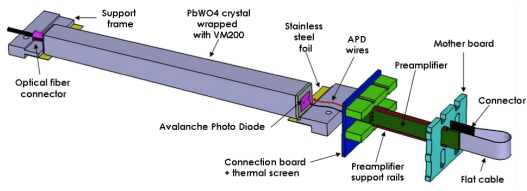


Figure 6: A schematic view of an ECal module.

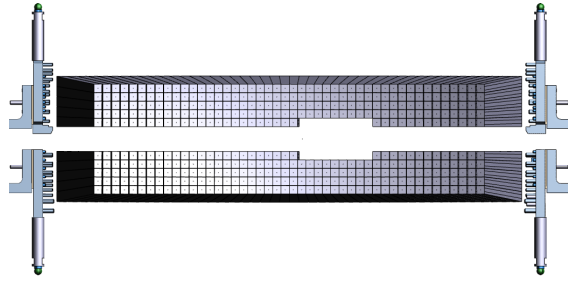


Figure 7: Rendered layout view of the ECal looking downstream.

377 silicon sensors correct to within a few hundred microns
 378 measured from tracks in the HPS Test Run data. A more
 379 sophisticated global track-based alignment technique to
 380 reach final alignment precision well below $50\text{ }\mu\text{m}$ is be-
 381 ing developed.

382 5. Electromagnetic Calorimeter

383 The electromagnetic calorimeter (ECal), installed
 384 downstream of the PS dipole magnet, performs two es-
 385 sential functions for the experiment: it provides a trigger
 386 signal to select what events to read out from the detector
 387 sub-systems and is used in the analysis to identify elec-
 388 trons and positrons. The technology and design choices
 389 are largely driven by the need for a compact forward de-
 390 sign covering the SVT A' acceptance and able to fully
 391 absorb electrons and positrons with energy between 0.5-
 392 6.5 GeV, fine granularity and signal readout speed to
 393 handle $1\text{ MHz}/\text{cm}^2$ of electromagnetic background and
 394 be radiation hard. The PbWO₄ crystal inner calorime-
 395 ter of the CLAS detector [15], in operation since 2005
 396 in Hall B, meets all the requirements set by HPS. The
 397 modules from this calorimeter have been subsequently
 398 repurposed for HPS.

399 5.1. Components

400 The ECal module shown in Figure 6 is based on a
 401 tapered 160 mm long PbWO₄ crystal with a $13.3 \times$
 402 13.3 mm^2 ($16 \times 16\text{ mm}^2$) front (rear) face wrapped in
 403 VM2000 multilayer polymer mirror film. The scintilla-
 404 tion light, approximately 3 photoelectrons/MeV, is read
 405 out by a $5 \times 5\text{ mm}^2$ Hamamatsu S8664-55 Avalanche
 406 Photodiode (APD) with 75% quantum efficiency glued
 407 to the rear face surface using MeltMount 1.7 thermal
 408 plastic adhesive. The low gain of APDs (~ 200) was
 409 compensated with custom-made preamplifier boards,
 410 which provide a factor of 2333 amplification of the APD
 411 signal.

412 5.2. Layout

413 Similar to the SVT, the ECal is built in two separate
 414 halves that are mirror reflections of one another about
 415 the plane of the nominal electron beam to avoid inter-
 416 fering with the 15 mrad “dead zone”. As shown in
 417 Figure 7, the 221 modules in each half, supported by
 418 aluminum support frames, are arranged in rectangular
 419 formation with 5 layers and 46 crystals/layer except for
 420 the layer closest to the beam where 9 modules were re-
 421 moved to allow a larger opening for the outgoing elec-
 422 tron and photon beams. Each half was enclosed in a
 423 temperature controlled box ($< 1^\circ\text{ F}$ stability and $< 4^\circ\text{ F}$
 424 uniformity) to stabilize the crystal light yield and the op-
 425 eration of the APDs and its preamplifiers. Four printed
 426 circuit boards mounted on the backplane penetrated the
 427 enclosure and were used to supply the $\pm 5\text{ V}$ operating
 428 voltage for the preamplifiers, 400 V bias voltage to the
 429 APDs, and to read out signals from the APDs. Each half
 430 of the ECal was divided into 12 bias voltage groups with
 431 a gain uniformity of about 20%.

432 During the HPS Test Run, both halves were held in
 433 place by four vertical bars attached to an above rail,
 434 placing the front face of the crystals 147 cm from the
 435 upstream edge of the magnet and with a 8.7 cm gap
 436 between the innermost edge of the crystals in the two
 437 halves.

438 5.3. Signal readout

439 After a 2:1 signal splitter, 1/3 of an amplified APD
 440 signal was fed to a single channel of a JLab flash ADC
 441 (FADC) board [16]. 2/3 of the signal was sent to a
 442 discriminator module and then to a TDC for a timing
 443 measurement. The FADC boards are high speed VXS
 444 modules digitizing up to 16 APD signals at 250 MHz
 445 and storing samples in $8\text{ }\mu\text{s}$ deep pipelines with 12-bit
 446 resolution. When a trigger is received, the part of the
 447 pipeline from 5 samples before and 30 after the signal
 448 which crossed a programmable threshold (for the HPS

449 Test Run this was set to ≈ 70 MeV) are summed and
 450 stored in a 17-bit register for readout. In addition a
 451 4 ns resolution timestamp of the threshold crossing is
 452 reported in the readout for each pulse. This scheme
 453 significantly compresses the data output of the FADC.
 454 During offline data analysis, a calibrated pedestal value
 455 is subtracted to obtain the actual summed energy. Two
 456 20-slot VXS crates with 14 (13) FADC boards were em-
 457 ployed in the HPS Test Run to read out the top (bottom)
 458 half of the ECal. In the HPS Test Run 385 out of 442
 459 modules (87%) were used in offline reconstruction, 39
 460 modules were disabled or not read out (no FADC chan-
 461 nel available, no APD bias voltage or masked out due
 462 to excessive noise) and 18 were masked offline due to
 463 noise.

464 6. Trigger and Data Acquisition

465 The DAQ system handles acquisition of data from the
 466 ECal and SVT sub-detectors with two DAQ architec-
 467 tures. The SVT DAQ is based on Advanced Telecom
 468 Communications Architecture (ATCA) hardware while
 469 the ECal uses VMEbus Switched Serial (VXS) based
 470 hardware. Data from the sub-detectors are only read-
 471 out when a trigger signal from the trigger system is re-
 472 ceived.

473 6.1. Trigger system

474 The trigger system is designed to select time coinci-
 475 dences of electromagnetic clusters in the top and bot-
 476 tom halves of the ECal. Figure 8 shows a schematic
 477 overview of each stage of the system. Each channel on
 478 the FADC board has an independent data path to send 5-
 479 bit pulse energy and 3-bit pulse arrival time information
 480 every 32 ns to a trigger processing board (CTP), which
 481 is in the same crate. The 3-bit pulse arrival time allows
 482 the trigger to know the pulse timing at 4 ns resolution.
 483 Contrary to the readout path described in Sec. 5.3, this
 484 energy is a pedestal-subtracted time-over-threshold sum

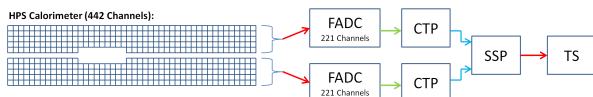


Figure 8: Block diagram of the ECAL trigger system consisting of the FADC that samples and digitizes signals for each detector channel and sends them for cluster finding in the CTP. The CTP clusters are sent to the SSP where the final trigger decision is taken based on pairs of clusters in both halves of the ECal. The decision is sent to the Trigger Supervisor (TS) that generates the necessary signals to readout the sub-detectors.

485 with programmable offsets and minimum threshold dis-
 486 criminator for each channel. With input from all FADC
 487 channels, i.e. one half of the ECal, the CTP performs
 488 cluster finding and calculates cluster energy and tim-
 489 ing information. The 3x3 fixed-window, highly parallel,
 490 FPGA-based cluster algorithm simultaneously searches
 491 for up to 125 clusters with energy sum larger than the
 492 programmable energy threshold (≈ 270 MeV). Crystals
 493 in the fixed-window are included in the sum if the lead-
 494 ing edge of the pulse occurred within a 32 ns time win-
 495 dow to take into account clock skew and jitter through-
 496 out the system. The CTP only accepts clusters with the
 497 highest energy 3x3 window locally to deal with over-
 498 lapping and very large clusters. The sub-system board
 499 (SSP) receives the clusters from the top and bottom half
 500 CTP at a maximum of 250MHz and searches for pairs
 501 of clusters in a 8 ns wide coincidence window. The SSP
 502 sends triggers to the trigger supervisor (TS), which gen-
 503 erates all the necessary signals and controls the entire
 504 DAQ system readout through the trigger interface units
 505 installed in every crate that participate in the readout
 506 process.

507 The trigger system is free-running and driven by the
 508 250 MHz global clock and has essentially zero dead
 509 time at the occupancies expected for HPS. The trigger
 510 supervisor can apply dead time if necessary, for exam-
 511 ple on a ‘busy’ or ‘full’ condition from the front-end
 512 electronics. The system is designed to handle trigger
 513 rates above 50 kHz and has a latency set to $\approx 3 \mu\text{s}$ to
 514 match that required by the SVT APV25 ASIC. During
 515 the HPS Test Run, for the most part the trigger system
 516 required only a single cluster in either the top or bot-
 517 tom Ecal halves and was tested to trigger rates above
 518 100 kHz by lowering thresholds.

519 6.2. SVT Data Acquisition

520 The SVT DAQ is based on the Reconfigurable Clus-
 521 ter Element (RCE) and cluster interconnect concept de-
 522 veloped at SLAC as generic building blocks for DAQ
 523 systems. The RCE is a generic computational build-
 524 ing block, housed on a separate daughter card called
 525 Data Processing Module (DPM), that are realized on an
 526 ATCA front board called the Cluster On Board (COB),
 527 see Figure 9. The first generation RCE used in the HPS
 528 Test Run consisted of a Virtex 5 FPGA with 1 GB of
 529 DDR3 RAM. A schematic overview of the system is
 530 shown in Figure 10. The analog outputs of up to 12
 531 SVT half-modules (60 APV25 ASICs) are digitized on
 532 the Rear-Transition-Module (RTM), a custom board on
 533 the back side of the ATCA crate, interfacing the HPS-
 534 specific readout to the generic DAQ components on the
 535 COB. A pre-amplifier converts the APV25 differential



Figure 9: The SVT DAQ COB board with four data processing daughter cards (DPMs) visible on the left side.

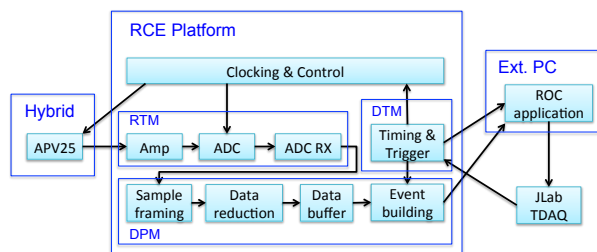


Figure 10: Block diagram overview of the SVT DAQ.

536 current output to a different voltage output scaled to the
 537 sensitive range of a 14-bit ADC operating at the system
 538 clock of 41.667 MHz. The RTM is organized into four
 539 sections with each section supporting three SVT half-
 540 module hybrids (15 APV25 ASICs). The RTM also in-
 541 cludes a 4-channel fiber optic module and supporting
 542 logic which is used to interface to the JLab trigger sys-
 543 tem supervisor. Each section of the RTM is input to a
 544 DPM which applies thresholds for data reduction and
 545 organizes the sample data into UDP datagrams. The
 546 DPM also hosts an I²C controller used to configure and
 547 monitor the APV25 ASICs. A single ATCA crate with
 548 two COB cards was used, one supporting four DPMs
 549 and one supporting 3 DPMs and one DPM that is con-
 550 figured as the trigger and data transmission module. The
 551 two COB cards and their DPMs are interconnected with
 552 a 10 Gb/s switch card [17] which also hosts two 1Gb/s
 553 Ethernet interfaces to the external SVT DAQ PC.

554 The external PC supports three network interfaces;
 555 two standard 1 Gb/s Ethernet and one custom low-
 556 latency data reception card. The first is used for slow
 557 control and monitoring of the 8 DPM modules and the
 558 second serves as the interface to the JLAB data acquisi-
 559 tion system. The third custom low-latency network in-
 560 terface is used to receive data from the ATCA crate and
 561 supports a low latency, reliable TTL trigger acknowl-

562 edge interface to the trigger DPM. This PC hosts the
 563 SVT control and monitoring software as well as the
 564 Read Out Controller application used to interface with
 565 the JLab DAQ.

566 In order to minimize cable length for the analog
 567 APV25 output signal the ATCA crate was located ap-
 568 proximately 1 m from the beam line, next to our cab-
 569 ble vacuum feed-troughs. Before shielding with lead-
 570 blankets was arranged, we observed two failures of
 571 normally reliable ATCA crate power supplies, time-
 572 correlated to beam instabilities.

573 Although trigger rates during the HPS Test Run were
 574 significantly lower, this system was tested at trigger
 575 rates up to 20 kHz and 50 MB/s.

6.3. General Data Acquisition and Online Computing

577 Every crate participating in the readout process con-
 578 tains a Readout Controller (ROC) that collects digitized
 579 information, processes it, and sends it on to the event
 580 builder. For the ECal, both VXS crates run ROC ap-
 581 plications in a single blade Intel-based CPU module run-
 582 ning CentOS Linux OS. For the SVT DAQ, the ROC
 583 application runs on the external PC under RHEL. The
 584 event builder assembles information from the ROCs into
 585 a single event which is passed to the event recorder that
 586 writes it to a RAID5-based data storage system capa-
 587 ble of handling up to 100 MB/s. The event builder and
 588 other critical components run on multicore Intel-based
 589 multi-CPU servers. The DAQ network system is a net-
 590 work router providing 10 Gb/s high-speed connection to
 591 the JLab computing facility for long-term storage. For
 592 the HPS Test Run, both the SVT and ECal ROC had a
 593 1 Gb/s link to the network router.

7. Reconstruction and Performance

7.1. SVT Performance

594 For the duration of the HPS Test Run all SVT mod-
 595 ules and APV25 chips were configured to their nominal
 596 operating points [18] with all sensors reverse-biased at
 597 180 V. The sensors were operated within a temperature
 598 range of 20 – 24°C. Approximately 97% of the 12,780
 599 SVT channels were found to be operating normally; the
 600 fraction of dead or noisy channels varied from 2.4%
 601 to 4.7% throughout the HPS Test Run. Most of these
 602 losses were due to 2-4 misconfigured APV25 ASICs, a
 603 known noisy half-module and problems in two particu-
 604 lar APV25 ASICs.

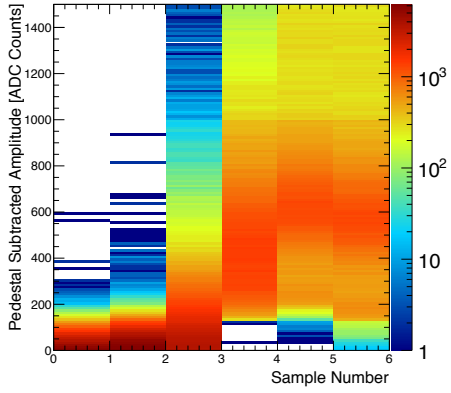


Figure 11: Accumulation of six pedestal-subtracted samples from individual SVT channels associated with hits on tracks.

607 7.1.1. Cluster and Hit Reconstruction

608 After a trigger is received, the amplitude of every
 609 APV25 analogue output is sampled and digitized in
 610 six consecutive time bins, separated by roughly 25 ns.
 611 The typical, pedestal subtracted, pulse shape obtained
 612 is shown in Figure 11. As the figure demonstrates, the
 613 SVT was well timed-in to the trigger with the rise of the
 614 pulse at the 3rd sampling point. In order to find the time,
 615 t_0 , and amplitude of each hit, the six samples from each
 616 channel are fitted to an ideal $CR - RC$ function. Note that
 617 in the HPS Test Run the APV25 ASICs were operating
 618 with a 50 ns shaping time. These hits are passed through
 619 a simple clustering algorithm which forms clusters by
 620 grouping adjacent strips with the position of a cluster on
 621 the sensor determined by the amplitude-weighted mean.
 622 With a linear gain up to ≈ 3 MIPs, the cluster charge
 623 for hits associated with a track follow the characteristic
 624 Landau shape. A noise level between $1.1 - 1.5 \times 10^3$
 625 electrons was established through multiple calibration
 626 runs giving a signal to noise ratio of 21 – 25. Lab-
 627 based radioactive source tests were used to provide the
 628 absolute charge normalization. After clustering hits on
 629 a sensor, the hit time for each cluster is computed as
 630 the amplitude-weighted average of the individually fit-
 631 ted t_0 on each channel. The t_0 resolution is studied by
 632 comparing the cluster hit time with the average of all
 633 cluster hit times on the track shown in Figure 13. After
 634 correcting for offsets from each sensor (time-of-flight
 635 and clock phase) and accounting for the correlation be-
 636 tween the t_0 and track time, the extracted t_0 resolution is
 637 2.6 ns. This is somewhat worse than the approximately
 638 2 ns resolution expected for S/N 25 which we attribute
 639 to the true pulse shape differing from our idealized fit

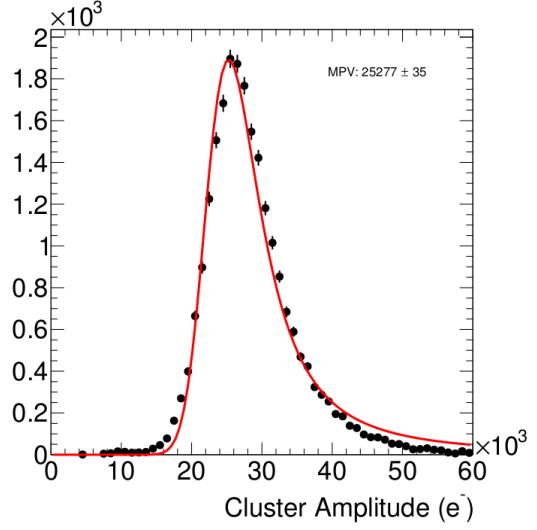


Figure 12: The cluster charge distribution for hits associated with track follow the characteristic Landau shape.

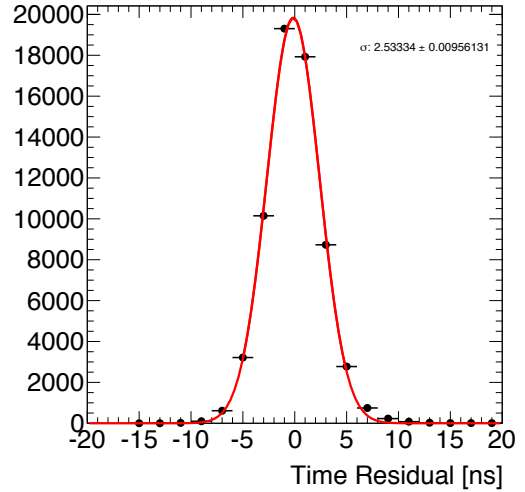


Figure 13: The residual of individual cluster times with the average of all clusters on the track.

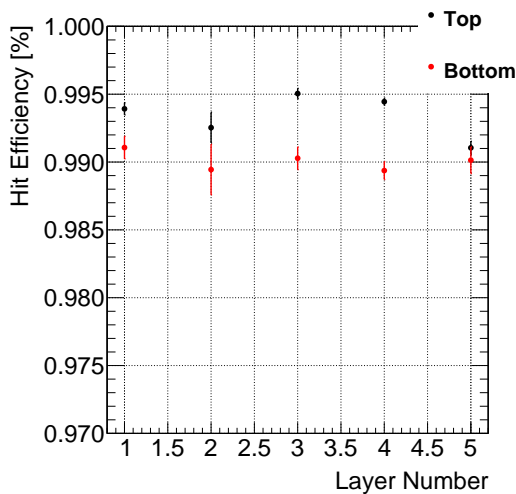


Figure 14: The hit reconstruction efficiency as a function of detector layer.

function which will be improved in the future. Reducing the APV25 ASIC pulse shaping time to 35 ns will also improve time resolution. These results show that we can operate with the six sample readout mode of the APV25 chip and achieve time resolution adequate for pileup rejection during electron running in HPS.

Good agreement was obtained between observed and simulated occupancies after taking into account dead or noisy channels. The hit reconstruction efficiency was estimated by measuring the number of good tracks with a hit close to the extrapolated intersection of a given sensor that was excluded from the track fit itself. Tracks which intersect regions with known bad channels or very close to the edge region are excluded. The hit reconstruction efficiency, see Figure 14, was measured to be above 98% and fairly uniform across the SVT.

The spatial resolution of similar microstrip sensors is well established by test beam data, against which the charge deposition model in the simulation is validated. This resolution can be parameterized as a function of the total signal to single-strip noise and the crossing angle of tracks through the sensor. The single-hit resolution for charged particles with signal to noise ratio above 20, as demonstrated here, is relatively constant at approximately $6 \mu\text{m}$ for tracks that enter approximately normal to the sensors as in HPS.

7.1.2. Momentum and Vertexing Resolution

By selecting e^+e^- pairs from the triggered events we are able to study basic distributions of pair production

kinematics. Pairs of oppositely charged tracks, one in the top and one in the bottom half of the SVT, with momentum larger than 400 MeV were selected. The pair production kinematics are relatively well reproduced as shown in Figure 15.

The expected momentum resolution from simulation is between 4-5% for tracks in the momentum range of the HPS Test Run. By comparing the shapes of the kinematic distributions for single- and two track events between data and simulation we estimate an agreement with the nominal scale and resolution to within 10%.

In the HPS Test Run, as well as in electron running with HPS, the dominant source of uncertainty in the tracking and vertexing is multiple Coulomb scattering. For the vertexing performance the foremost difference compared to electron beam running is that the target was located approximately 67 cm upstream from our nominal target position; giving almost collinear tracks in the detector. The increased lever arm over which tracks are extrapolated widens the resolution with up to a factor of eight (depending on momentum) compared to what is achieved at the nominal electron target position for HPS. Figure 16 shows the horizontal and vertical positions of the extrapolated track at the converter position. While residual alignments show small shifts, the good agreement between data and simulated events of the widths indicates a good understanding of the material budget and distribution in the SVT. Having the dominant contribution to the vertex resolution approximately right demonstrates that the resolution in HPS, with a target at 10 cm, will be as calculated.

7.2. ECal Performance

The integrated pulse of each FADC channel was converted to energy by subtracting a pedestal and applying a conversion factor to convert ADC counts to energy. The pedestals are measured using special runs where each trigger records 100 samples of signals from the APDs with 4 ns between each sample. The pedestals were extracted from the part of the window before the actual hit in the calorimeter. Modules with signal above the threshold are clustered using a simple algorithm similar to the one deployed for the trigger (see Sec. 6.1). Due to the high effective readout threshold of 73 MeV the average number of crystals in a cluster was ~ 3 and the simple clustering algorithm worked well for reconstruction of the detected shower energy. An average noise level of approximately 15 MeV was measured in special pedestal runs.

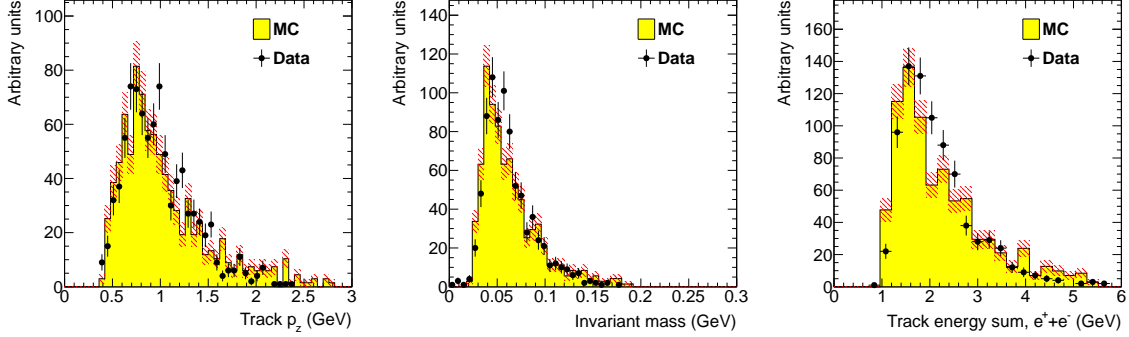


Figure 15: Kinematic distributions for $e^+ e^-$ pairs selected by opposite charged tracks in the top and bottom half of the tracker: track momentum in the top half of the SVT (left), invariant mass (middle) and the sum of the track momentum for the pair (right).

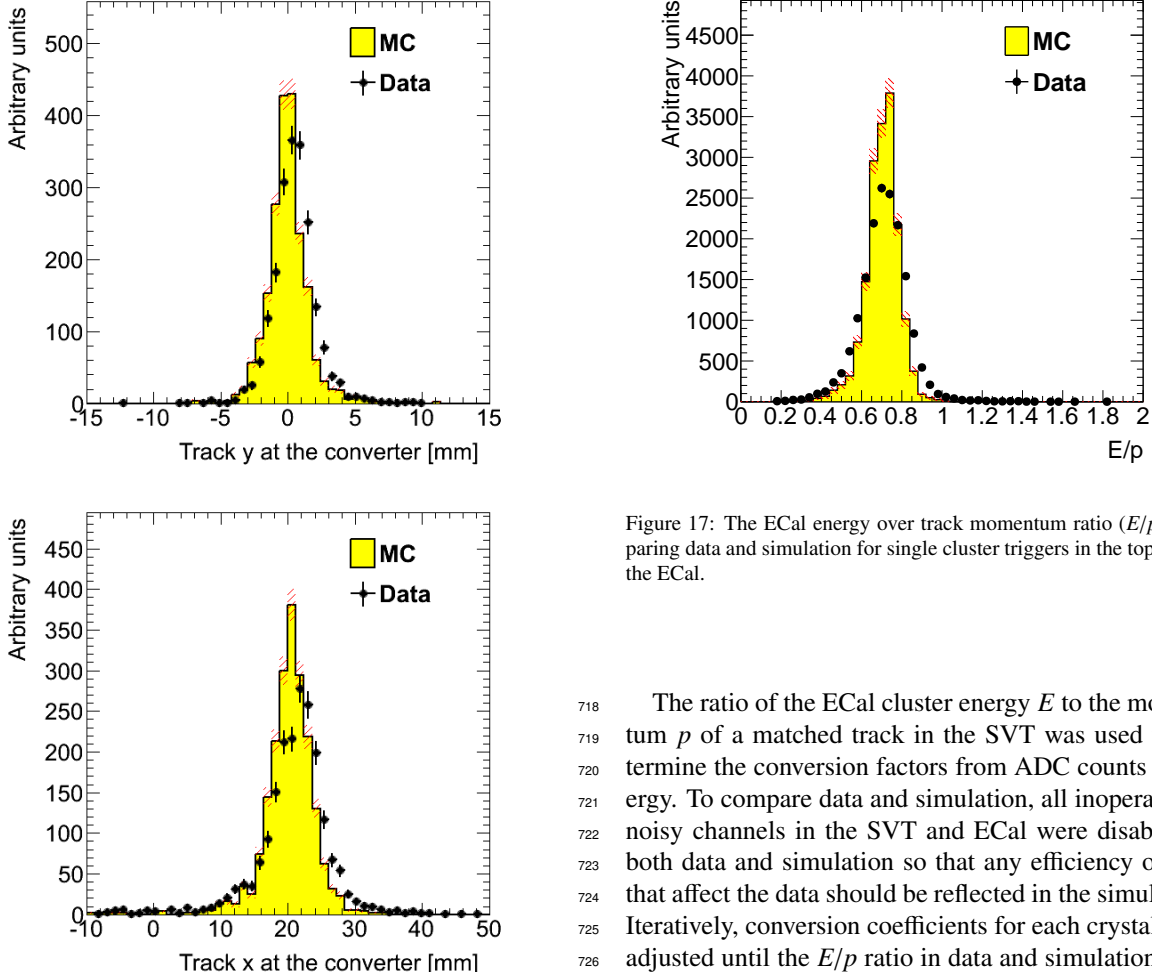


Figure 16: Vertical (top) and horizontal (bottom) extrapolated track position at the converter taking into account the measured fringe field.

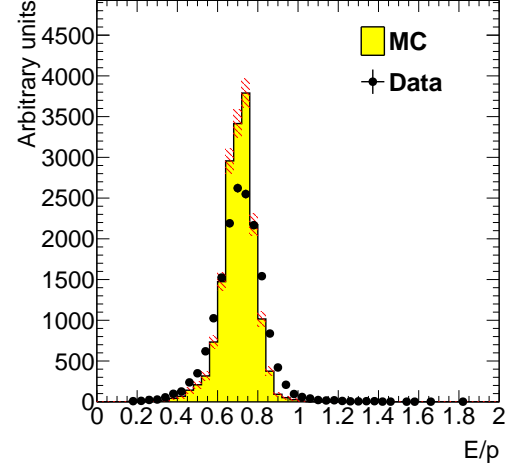


Figure 17: The ECal energy over track momentum ratio (E/p) comparing data and simulation for single cluster triggers in the top half of the ECal.

The ratio of the ECal cluster energy E to the momentum p of a matched track in the SVT was used to determine the conversion factors from ADC counts to energy. To compare data and simulation, all inoperable or noisy channels in the SVT and ECal were disabled in both data and simulation so that any efficiency or bias that affect the data should be reflected in the simulation. Iteratively, conversion coefficients for each crystal were adjusted until the E/p ratio in data and simulation were similar. The distribution of the E/p ratio in data and simulation are compared in Figure 17. The peak position of the distribution indicates the sampling fraction of the ECal, the fraction of the incident particle energy measured in the cluster. The width and tails of the distri-

bution in data indicates imperfect calibration and noise of the ECal modules. This level of calibration and the agreement with simulation was found to be sufficient to study normalized event rates in the HPS Test Run.

7.3. Trigger Performance

As described above in Sec. 6, the energy from each crystal is measured differently in the trigger and what is readout from the ECal. The trigger performance was studied by simulating the trigger for each event and comparing to how the events were actually triggered. To eliminate trigger bias, we use a tag and probe method: to study the trigger performance in one half of the ECal, we select events which triggered the other half and where there was exactly one probe cluster in the ECal half under study. We then measure trigger efficiency as the fraction of tagged events that fired the trigger in the probe half as a function of the probe cluster energy, shown in Figure 18. The trigger turn-on is

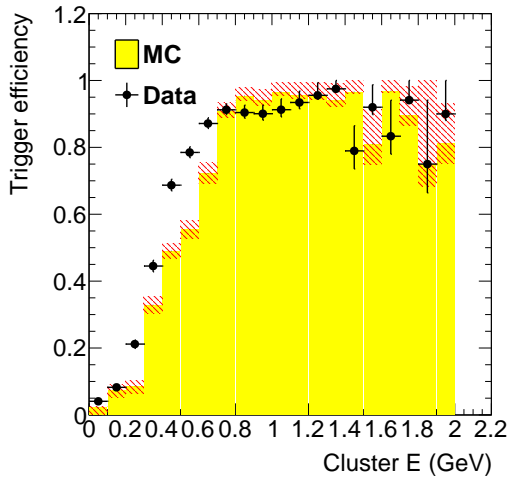


Figure 18: Trigger efficiency in both halves of the ECal for data and simulation as a function of cluster energy.

slow and reaches an uneven plateau just below 1 GeV for two reasons; gain variations between different crystals lead to the threshold variations and the nonlinearity of the time-over-threshold integral means that the effective threshold is higher for clusters that span multiple crystals. The effective trigger threshold is therefore dependent on position and energy of the particle as well as cluster multiplicity.

As a cross-check we simulate the FADC trigger path by converting from readout hits (with fixed-size window integration) to trigger hits (time-over-threshold integration). The CTP clustering algorithm and the trigger

Converter (% X_0)	1.60	0.45	0.18
EGS5	1162 ± 112	255 ± 28	94 ± 17
GEANT4	2633 ± 250	371 ± 38	114 ± 18
Observed	1064 ± 2	196 ± 1	92 ± 1

Table 4: Observed and predicted event rate (in Hz) normalized to 90 nA for three different converter thicknesses. The uncertainty on the prediction includes systematic uncertainties from ECal alignment, background normalization, beam current normalization and limited statistics in the simulation.

decision from the SSP are simulated before we compare the trigger decision and trigger time to what was reported by the actual trigger. For every event, the trigger reports the trigger decision as a bit mask (top half, bottom half or both) and the time the trigger fired. The turn-on from the trigger threshold was measured to be 1280 in units of ADC counts as expected. The threshold was not perfectly sharp because of uncertainties in the conversion from readout to trigger hits described above, but based on comparisons with simulation we found that the trigger worked exactly as specified.

7.4. Trigger Rate Comparisons

Trigger rates observed in the HPS Test Run are dominated by multiple Coulomb scattered e^+e^- pairs in the converter. In simulated events, the rate of triggers depend on the modeling of the pairs angular distribution and the subsequent multiple Coulomb scattering in the converter. Rates from different converter thicknesses are used to study the varying multiple Coulomb scattering contribution (pair production angle is constant). Restricting clusters to a well calibrated region of the ECal and subtracting the “no converter” background we see agreement with the rates predicted by the EGS5 simulation program, see Table 7.4. This gives further confidence that the dominant source of background occupancy for HPS, multiple Coulomb scattered beam electrons, is well described [19, 20, 21].

8. Summary and Outlook

The HPS Test Run experiment, using a simplified version of the apparatus planned for the full HPS experiment in a parasitic photon beam, demonstrated the feasibility of the detector technologies proposed for the silicon vertex tracker, electromagnetic calorimeter, and data acquisition systems. Performance from each of these subsystems has been shown to be adequate to conduct the full experiment successfully. Studies of multiple Coulomb scattering tails of electrons and positrons from photon conversions further backs expectations from simulation, giving credence to estimates

801 of the detector backgrounds expected in electron beam
802 running for HPS.

803 9. Acknowledgements

804 The authors are grateful for the support from Hall B
805 at JLab and especially the Hall B engineering group for
806 support during installation and decommissioning. They
807 also would like to commend the CEBAF personnel for
808 good beam performance, especially the last few hours
809 of operating CEBAF6. The tremendous support from
810 home institutions and supporting staff also needs praise
811 from the authors.

812 This work has been supported by the US Department
813 of Energy.

- 856 [16] D. H., et al., Integrated tests of a high speed VXS
857 switch card and 250 MSPS flash ADCs, 2007.
858 doi:10.1109/NSSMIC.2007.4436457.
859 [17] R. Larsen, Emerging New Electronics Standards for Physics,
860 Conf.Proc. C110904 (2011) 1981–1985.
861 [18] L. Jones, APV25-S1: User guide version 2.2, RAL Microelec-
862 tronics Design Group, 2011.
863 [19] D. Attwood, P. Bell, S. Bull, T. McMahon, J. Wilson, et al.,
864 The scattering of muons in low Z materials, Nucl.Instrum.Meth.
865 B251 (2006) 41–55.
866 [20] G. Shen, C. Ankenbrandt, M. Atac, R. M. Brown, S. Ecklund,
867 et al., Measurement of Multiple Scattering at 50-GeV/c to 200-
868 GeV/c, Phys.Rev. D20 (1979) 1584.
869 [21] B. Gottschalk, A. Koehler, R. Schneider, J. Sisterson, M. Wag-
870 ner, Multiple coulomb scattering of 160 mev protons, Nuclear
871 Instruments and Methods in Physics Research Section B: Beam
872 Interactions with Materials and Atoms 74 (1993) 467 – 490.

814 References

- 815 [1] B. Holdom, Two U(1)'s and Epsilon Charge Shifts, Phys.Lett.
816 B166 (1986) 196.
817 [2] R. Essig, J. A. Jaros, W. Wester, P. H. Adrian, S. Andreas, et al.,
818 Dark Sectors and New, Light, Weakly-Coupled Particles (2013).
819 [3] M. Pospelov, Secluded U(1) below the weak scale, Phys.Rev.
820 D80 (2009) 095002.
821 [4] O. Adriani, et al. (PAMELA Collaboration), An anomalous
822 positron abundance in cosmic rays with energies 1.5-100 GeV,
823 Nature 458 (2009) 607–609.
824 [5] M. Ackermann, et al. (Fermi LAT Collaboration), Measure-
825 ment of separate cosmic-ray electron and positron spectra with
826 the Fermi Large Area Telescope, Phys.Rev.Lett. 108 (2012)
827 011103.
828 [6] M. Aguilar, et al. (AMS Collaboration), First Result from the
829 Alpha Magnetic Spectrometer on the International Space Sta-
830 tion: Precision Measurement of the Positron Fraction in Pri-
831 mary Cosmic Rays of 0.5350 GeV, Phys.Rev.Lett. 110 (2013)
832 141102.
833 [7] N. Arkani-Hamed, D. P. Finkbeiner, T. R. Slatyer, N. Weiner, A
834 Theory of Dark Matter, Phys.Rev. D79 (2009) 015014.
835 [8] J. D. Bjorken, R. Essig, P. Schuster, N. Toro, New Fixed-Target
836 Experiments to Search for Dark Gauge Forces, Phys.Rev. D80
837 (2009) 075018.
838 [9] A. G. et al. (HPS Collaboration), HPS Heavy Photon Search
839 Proposal, 2010.
840 [10] A. Sandorfi, et al., 2012. URL:
841 http://www.jlab.org/exp_prog/proposals/06/PR-06-101.pdf.
842 [11] I. Rashevskaya, S. Bettarini, G. Rizzo, L. Bosisio, S. Dittongo,
843 et al., Radiation damage of silicon structures with electrons of
844 900-MeV, Nucl.Instrum.Meth. A485 (2002) 126–132.
845 [12] D. S. Denisov, S. Soldner-Rembold, D0 Run IIB Silicon Detec-
846 tor Upgrade: Technical Design Report (2001).
847 [13] M. French, L. Jones, Q. Morrissey, A. Neviani, R. Turchetta,
848 et al., Design and results from the APV25, a deep sub-micron
849 CMOS front-end chip for the CMS tracker, Nucl.Instrum.Meth.
850 A466 (2001) 359–365.
851 [14] M. Friedl, C. Irmler, M. Pernicka, Readout of silicon strip detec-
852 tors with position and timing information, Nucl.Instrum.Meth.
853 A598 (2009) 82–83.
854 [15] A. Radyushkin, P. Stoler (Eds.), Inner Calorimeter in Clas/dvcs
855 Experiment, 2008.